

11. Kotegawa, H. *et al.* Evidence for strong-coupling *s*-wave superconductivity in MgB_2 : ^{11}B NMR study. *Phys. Rev. Lett.* **87**, 127001 (2001).
12. Ishida, K. *et al.* Spin-triplet superconductivity in Sr_2RuO_4 identified by ^{17}O Knight shift. *Nature* **396**, 658–660 (1998).
13. Wolfer, W. G. Radiation effects in plutonium. *Los Alamos Sci.* **26**, 274–285 (2000).
14. Kitaoka, Y. *et al.* Nuclear relaxation and Knight shift studies of copper in $\text{YBa}_2\text{Cu}_3\text{O}_{7-y}$. *J. Phys. Soc. Jpn* **57**, 30–33 (1988).
15. Kohori, Y. *et al.* NMR and NQR studies of the heavy fermion superconductors CoTiIn_5 ($T = \text{Co}$ and Ir). *Phys. Rev. B* **64**, 134526 (2001).
16. Ishigaki, A. & Moriya, T. Nuclear magnetic relaxation around the magnetic instability in metals. *J. Phys. Soc. Jpn* **65**, 3402–3403 (1996).
17. Bauer, E. D. *et al.* Structural tuning of unconventional superconductivity in PuMGa_5 ($M = \text{Co, Rh}$). *Phys. Rev. Lett.* **93**, 147005 (2004).
18. Moriya, T. & Ueda, K. Antiferromagnetic spin fluctuations and superconductivity. *Rep. Prog. Phys.* **66**, 1299–1341 (2003).
19. Bang, Y. *et al.* T_{C} in the *d*-wave superconducting state with coexisting antiferromagnetism. *Phys. Rev. B* **69**, 014505 (2004).
20. Hirschfeld, P. J. *et al.* Consequences of resonant impurity scattering in anisotropic superconductors: thermal and spin properties. *Phys. Rev. B* **37**, 83–97 (1988).
21. Abrikosov, A. A. *et al.* *Methods of Quantum Field Theory in Statistical Physics* Ch. 7, Sec. 39.3 (Dover, New York, 1975).
22. Bang, Y. *et al.* Possible pairing mechanisms of PuCoGa_5 superconductor. *Phys. Rev. B* **70**, 104512 (2004).
23. Opahle, I. & Oppeneer, P. M. Superconductivity caused by the pairing of plutonium 5*f* electrons in PuCoGa_5 . *Phys. Rev. Lett.* **90**, 157001 (2003).
24. Colineau, E. *et al.* Magnetic and electronic properties of the antiferromagnet NpCoGa_5 . *Phys. Rev. B* **69**, 184411 (2004).
25. Griveau, J. C. *et al.* Pressure dependence of the superconductivity in PuCoGa_5 . *J. Magn. Magn. Mater.* **272/276**, 154–155 (2004).
26. Savrasov, S. Y. & Kotliar, G. Ground state theory of δ -Pu. *Phys. Rev. Lett.* **84**, 3670–3673 (2000).
27. Kawasaki, Y. *et al.* Anisotropic spin fluctuations in heavy-fermion superconductor CeCoIn_5 : In-NQR and Co-NMR studies. *J. Phys. Soc. Jpn* **72**, 2308–2311 (2003).

Supplementary Information accompanies the paper on www.nature.com/nature.

Acknowledgements We thank Z. Fisk, D. Pines and C. P. Slichter for discussions. This work was performed at Los Alamos National Laboratory under the auspices of the US Department of Energy Office of Science. Y.B. is supported by KOSEF through CSCMR.

Competing interests statement The authors declare that they have no competing financial interests.

Correspondence and requests for materials should be addressed to N.J.C. (curro@lanl.gov).

Two-dimensional spectroscopy of electronic couplings in photosynthesis

Tobias Brixner¹, Jens Stenger¹, Harsha M. Vaswani¹, Minhaeng Cho², Robert E. Blankenship³ & Graham R. Fleming¹

¹Department of Chemistry, and the Institute for Quantitative Biomedical Research (QB3), University of California, Berkeley, and Physical Biosciences Division, Lawrence Berkeley National Laboratory, Berkeley, California 94720, USA

²Department of Chemistry and Center for Multidimensional Spectroscopy, Division of Chemistry and Molecular Engineering, Korea University, Seoul 136-701, Korea

³Department of Chemistry and Biochemistry, Arizona State University, Tempe, Arizona 85287, USA

Time-resolved optical spectroscopy is widely used to study vibrational and electronic dynamics by monitoring transient changes in excited state populations on a femtosecond timescale¹. Yet the fundamental cause of electronic and vibrational dynamics—the coupling between the different energy levels involved—is usually inferred only indirectly. Two-dimensional femtosecond infrared spectroscopy based on the heterodyne detection of three-pulse photon echoes^{2–7} has recently allowed the direct mapping of vibrational couplings, yielding transient

structural information. Here we extend the approach to the visible range^{3,8} and directly measure electronic couplings in a molecular complex, the Fenna–Matthews–Olson photosynthetic light-harvesting protein^{9,10}. As in all photosynthetic systems, the conversion of light into chemical energy is driven by electronic couplings that ensure the efficient transport of energy from light-capturing antenna pigments to the reaction centre¹¹. We monitor this process as a function of time and frequency and show that excitation energy does not simply cascade stepwise down the energy ladder. We find instead distinct energy transport pathways that depend sensitively on the detailed spatial properties of the delocalized excited-state wavefunctions of the whole pigment–protein complex.

The Fenna–Matthews–Olson (FMO) bacteriochlorophyll *a* (BChl) protein of green sulphur bacteria serves both as an antenna for collecting light energy and as a mediator for directing light excitations from the chlorosome antenna to the reaction centre^{9–12}. The FMO protein is a trimer of identical subunits, each containing seven BChl pigments. Because of its comparatively simple structure it is often employed as a model system for excitonic (delocalization) effects in photosynthesis research¹³. However, it is not clear to what extent individual spectral features, such as those in the linear FMO absorption spectrum, are caused by differences in site energies (arising from the interaction of the BChl pigments with their local protein environment) or by energy splitting from excitonic coupling (that is, pigment–pigment interaction)^{14–16}. With two-dimensional femtosecond spectroscopy, couplings can be made visible directly.

Two-dimensional (2D) optical spectroscopy^{3,8,17–21} measures the full nonlinear polarization of a quantum system in third order with respect to the field–matter interaction^{3,8,22}. A sequence of three ultrashort laser pulses excites the sample, and the emitted phase-matched signal field is detected in amplitude and phase as a function of optical frequency and the three experimentally controlled excitation–pulse time delays τ , T and t . Fourier transforms of the data^{8,21} reveal complex-valued 2D (ω_τ, ω_t) frequency maps of the system's response, where ω_τ and ω_t are the conjugate Fourier frequencies of τ and t . The real part can be interpreted as the transient field amplitude at a particular probe frequency ω_p , induced by a specific excitation frequency ω_τ after the waiting time (population time) T . The imaginary part describes transient changes in the refractive index. Whereas diagonal peaks in the 2D traces correspond to linear absorption positions, any off-diagonal contributions indicate coupling and, for $T > 0$, energy transfer. In the infrared regime, 2D maps for vibrational couplings have been determined^{2,4–7}, yielding transient structural information. Two-colour photon-echo spectroscopy has been used to study electronic coupling in a homodimer²³, but molecular cross-peak features for electronic transitions in the visible range have not yet been reported.

The experimental 2D trace of the FMO complex for $T = 0$ fs is shown in Fig. 1a. The positions of the three main diagonal peaks match the linear absorption spectrum below (Fig. 1d, solid black line). Elongation of these features along the diagonal indicates a correlation between excitation and emission frequencies within the same pigment and hence inhomogeneous spectral broadening^{2,24,25}. Analysis of the 2D contour shapes can recover the homogeneous linewidths. More importantly, however, several off-diagonal features (positive and negative) are clearly visible. Using an assignment of exciton levels (horizontal and vertical lines numbered 1–7 in Fig. 1a), one can qualitatively identify the extent of mutual correlations as the magnitude of the corresponding cross peaks. Quantitative evaluation is done by comparison with simulations as shown below. The cross-peak amplitude is determined by quantum-mechanical interference from different nonlinear optical transition pathways. Because of the electronic coupling between pigments, the excitonic transition dipoles become linear combinations of pigment

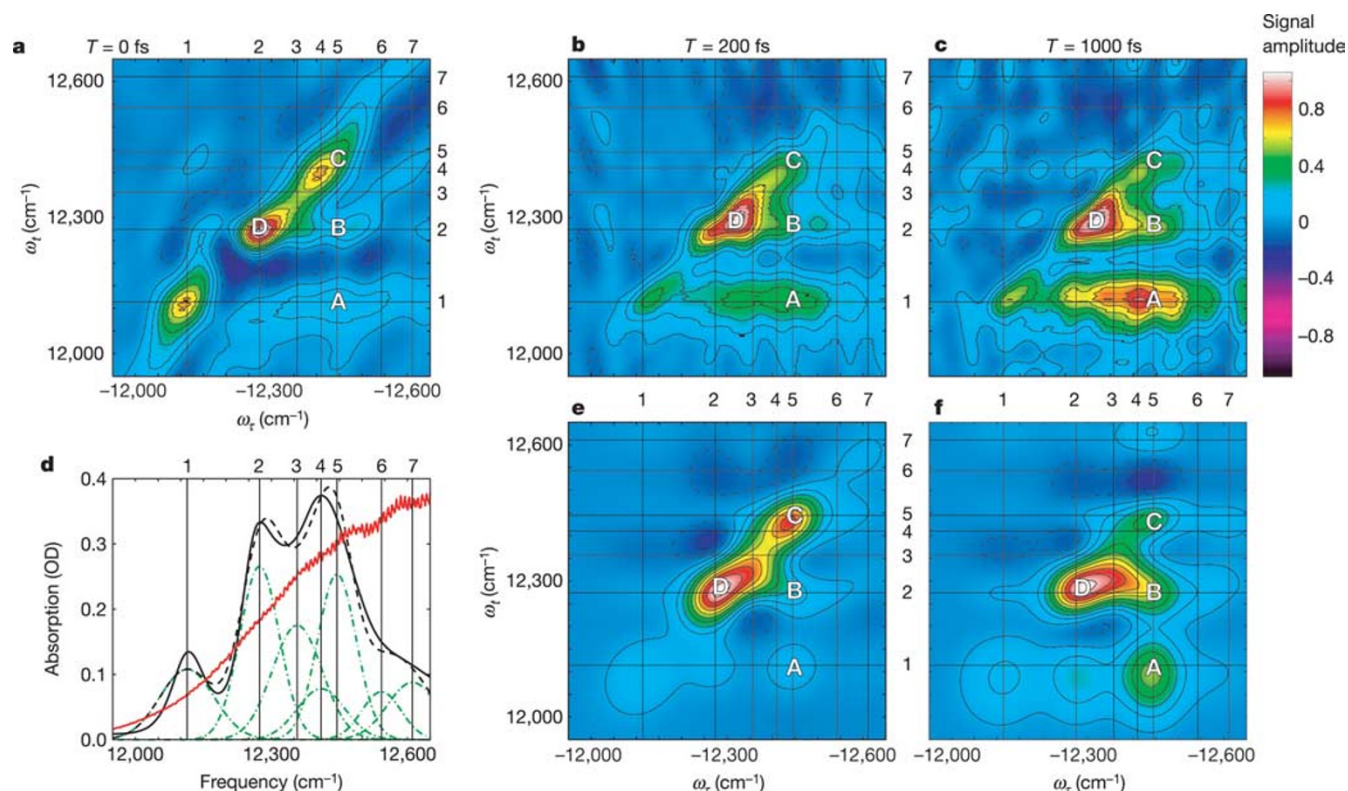


Figure 1 Experimental and theoretical spectra (real parts) of the FMO complex from *Chlorobium tepidum* at 77 K. **a–c**, The experimental 2D spectra (upper three panels) are shown for population times $T = 0$ fs (**a**), $T = 200$ fs (**b**) and $T = 1,000$ fs (**c**). Contour lines are drawn in 10% intervals at $\pm 5\%$, $\pm 15\%$, ..., $\pm 95\%$ of the peak amplitude, with solid lines representing positive contributions ('more light') and dashed lines negative features. Horizontal and vertical grid lines indicate exciton levels 1–7 as labelled. **d**, The

experimental linear absorption spectrum (solid black) is reproduced by theory (dashed black), with individual exciton contributions as shown (dashed–dotted green). The laser spectrum used in the 2D experiments (red) covers all transition frequencies. **e, f**, Simulations of 2D spectra are shown for $T = 200$ fs (**e**) and $T = 1,000$ fs (**f**). Off-diagonal features such as those labelled A and B are indicators of electronic coupling and energy transport; they are discussed in more detail in the text.

transition dipoles, and nonlinear optical transitions involving two different exciton states are allowed and produce off-diagonal peaks even at $T = 0$. The transitions above and below the diagonal involve different one-exciton and two-exciton states, with correspondingly different oscillator strengths. Accordingly, the cancellation between bleaching/stimulated emission features and excited-state absorption features is different in the two half-planes, giving rise to the stronger cross peaks below the diagonal. For cross peak A, the system is in an electronic coherence state of the ground and fifth excitonic states during τ and of the lowest one-exciton and ground states during t . This cross peak indicates that the BChl pigments that make up excitons 1 and 5 are coupled; feature B shows the same for excitons 2 and 5. The negative regions (dark blue in Fig. 1a) can be attributed to two-exciton contributions, that is, excited-state absorption.

The electronic couplings lead to energy transfer, which is observed for population times $T > 0$. As an example, we show two snapshots at $T = 200$ fs (Fig. 1b) and $T = 1,000$ fs (Fig. 1c). With these 2D spectra, not only do we measure the population evolution as in conventional pump–probe experiments, we also follow the state-to-state energy transfer pathway. Between 200 and 1,000 fs, the amplitude of the lowest-energy diagonal peak increases and the main diagonal peak (D) shifts to lower energies, indicating a sizeable downward population transfer. The concentration of features below the diagonal also indicates that 'downhill' transfer, from higher to lower energies, dominates. The cross peaks in Fig. 1b, c demonstrate the sensitivity of this method to pigment–pigment interactions. Focusing on the two dominant off-diagonal peaks near regions A and B, the 2D spectra show increasing amplitudes as

a function of waiting time T . This reveals, for example, the relaxation from exciton states 4 and 5 to exciton state 2 (B) and exciton state 1 (A) as a function of time. Other features can be discussed qualitatively in an analogous fashion.

For quantitative simulations we use a Frenkel exciton hamiltonian with electronic coupling constants and site energies obtained by fitting the resulting absorption and 2D spectra. A single ohmic spectral density (representing the chromophore–bath coupling-strength distribution) and modified Förster/Redfield theory^{26,27} are employed for fully self-consistent calculations of the exciton transfer rates, the linear absorption spectrum (Fig. 1d, dashed black line) and the time-dependent 2D spectra (Fig. 1e, f). By using modified Förster/Redfield theory, we can self-consistently describe the excited states as either localized or delocalized (excitonic) depending on the magnitude of the coupling constants²⁷. Most of the exciton states are delocalized over two or three molecules, but the lowest exciton is essentially localized on BChl 3 (refs 14, 28). The transport of excitation is treated as reversible; finite temperature and detailed balance are correctly incorporated. The comparison between experiment and theory shows that the positions of the peaks in the 2D frequency space are reproduced. In addition, the relative timescales associated with the appearance/disappearance of the specific features are also well described. For example, in both theory and experiment the amplitudes in cross peaks A and B increase with population time T as a result of downhill energy transfer. The experimental (and theoretical) ratios of the amplitude of cross peak B to diagonal peaks C and D at $T = 1$ ps are 1.49 (1.45) and 0.55 (0.5), respectively. The calculated relative amplitude of diagonal peak C to D (0.34) at $T = 1$ ps is also close to that from

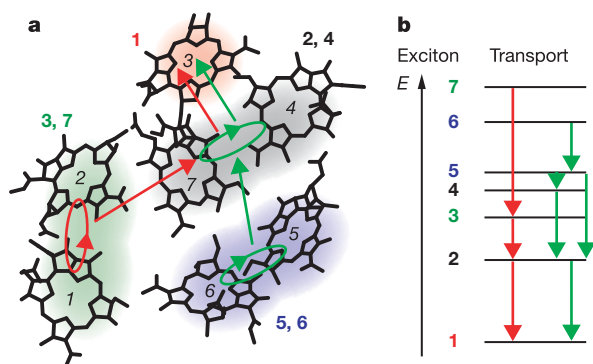


Figure 2 Exciton delocalization and energy transport. **a**, The FMO structural arrangement of the seven BChl molecules (italic numbers) is overlaid qualitatively with the delocalization patterns of the different excitons (coloured shading, bold numbers). Two main photoexcitation transfer pathways are indicated by red and green arrows. **b**, The energy transport is not just a simple process of stepwise energy decrease from one level to the next level below; rather, intermediate states are left out if they have insufficient spatial overlap with potential transfer partners.

experiment (0.37). We reproduce the presence of negative regions (dashed contour lines in Fig. 1c, f) corresponding to excited-state absorption to the two-exciton states, as well as the shape-contour change around the central diagonal peak, that is, its horizontal elongation towards region B. Some differences between experiment and simulation also occur. First, the build-up of cross peak A is slower in the simulations (Fig. 1f) than in experiment (Fig. 1c), implying that the calculated rate of populating level 1 is too slow; that is, the ratios of the amplitude of cross peak A to that of diagonal peaks C and D in the experimental (theoretical) spectra at $T = 1$ ps are 2.07 (1.41) and 0.76 (0.48), respectively. Second, the experimental cross peak near A (Fig. 1c) extends horizontally between exciton states 2 and 5, whereas in the simulation (Fig. 1f) separate peaks appear. This is at least partly the result of our limited (40 cm^{-1}) ω_T -frequency resolution.

Nevertheless, considering the complexity of the physical system, the agreement with the key 2D features is very promising. On the basis of our model, we now analyse how the excitation propagates between the different BChl molecules; that is, we follow the energy transfer in space and time. First we consider the delocalization of the exciton wavefunctions. Most excitons are delocalized mainly over only one or two neighbouring BChl molecules. This is indicated by the coloured shading in Fig. 2a. For example, excitons 3 and 7 (green, bold numbers) are both delocalized over the same BChls 1 and 2 (italic numbers). Second, from the exciton transfer-rate matrix obtained with the modified Förster/Redfield theory we can then identify the two major energy transport pathways shown by red and green arrows. In terms of energy levels, the results are displayed in Fig. 2b. An important factor for efficient energy transport is the mutual wavefunction overlap between initial and final states. Stronger overlap leads to faster transfer.

Consider first the 'green' pathway, starting with exciton 6 (on BChls 5 and 6). Because of its strong wavefunction overlap with exciton 5 (located on the same two pigments), the excitation is transferred efficiently (green ellipse). From there, exciton 4 can be reached, which in turn transfers to exciton 2 (again because of the strong spatial overlap as both excitons 2 and 4 are located on BChls 4 and 7). Alternatively, exciton 2 is reached directly from exciton 5. Note that in either case exciton 3 is not involved because it does not have strong spatial overlap with exciton 4 or 5. From exciton 2, the transport proceeds to exciton 1, and ultimately to the reaction centre where it is turned into chemical energy. The second pathway (red arrows) starts with exciton 7 and proceeds through excitons 3

and 2 to 1. Using similar arguments, it is clear that the good spatial overlap between excitons 7 and 3 and the weak coupling of corresponding BChls 1 and 2 to the remaining pigments prevents energy transfer from exciton 7 to excitons 4, 5 or 6. We conclude that the energy is not simply transferred stepwise down the energy ladder as has been conjectured previously^{15,28}. Instead, distinct pathways emerge (Fig. 2b) in which some energetically intermediate states are left out.

As illustrated by these findings, 2D femtosecond photon-echo spectroscopy remedies the deficiency of conventional types of spectroscopy in which only the evolutions of populations over time can be determined directly, but not the mechanisms that underlie these temporal changes. Thus we get detailed insight into the driving force of biological light harvesting, and applications to larger photosynthetic systems are possible. By noting that the magnitudes of electronic couplings and exciton relaxation rates are essentially dependent on the spatio-energetic distribution of chromophores, analysis of the exciton delocalization pattern leads to spatial information on the molecular scale. Hence, in general, the combination of these fully self-consistent calculations and experiments allows us to follow energy transport through space and time with nanometre spatial resolution and femtosecond temporal resolution. This methodology also opens the door to similar investigations of electronic couplings and energy transport in any photoactive assembly, macromolecule or other nanoscale system. □

Methods

Experiment and data analysis

Our implementation of inherently phase-stabilized two-dimensional Fourier-transform femtosecond spectroscopy for electronic transitions has been described in detail elsewhere^{20,21}. In brief, 50-fs, 805-nm, 3-kHz laser pulses from a home-built Tisapphire regenerative-amplifier laser system are used for three-pulse photon-echo spectroscopy in a diffractive-optic-based^{29,30} non-collinear four-wave mixing set-up with phase-matched box geometry. Time delays are introduced with better than $\lambda/100$ precision by movable glass wedges, and passive interferometric phase stability is maintained over several hours^{20,21}. The third-order signal is completely characterized by spectral interferometry with the help of a heterodyning local-oscillator pulse¹⁷. Automated subtraction of scattering terms removes experimental artefacts caused by sample imperfections. To resolve individual spectral features, we perform the experiment at low temperature (77 K) in a liquid-nitrogen cryostat (Oxford Instruments).

For any given population time (waiting time) T , the coherence time τ is scanned in 5-fs steps from -440 fs to $+440$ fs, moving excitation pulse 1 (2) in the second (first) half of the scanning period. Spectral interferograms are recorded with a 16-bit, 100-pixel \times 1,340-pixel, thermoelectrically cooled charge-coupled device camera (Princeton Instruments) and a 0.3-m imaging spectrometer (Acton). These parameters lead to a spectral resolution of 40 cm^{-1} for ω_T and 2 cm^{-1} for ω_L . The spot diameter at the sample position is $84 \mu\text{m}$ ($1/e^2$ intensity level), and the excitation energy is 20 nJ per pulse for the 2D traces shown. Repetitions with 30% of the laser power led to essentially the same results within the experimental uncertainties (though at decreased signal-to-noise ratio). Data analysis by Fourier transformation yields the desired 2D traces whose absolute phase is obtained by means of the projection-slice theorem and comparison with separately recorded spectrally resolved pump-probe data²¹. Each 2D trace is the average of three separate scans.

The FMO complex of *Chlorobium tepidum* was prepared in a buffer of 50 mM Tris HCl at pH 8.0 and 10 mM sodium ascorbate¹⁰. To avoid cracking of samples at low temperature, we used a water/glycerol (35:65 v/v) mixture between plastic windows (thickness 0.3 mm) with a 0.4 mm optical path length. The optical density peak value was 0.37 at 77 K. After each series of 2D scans for different population times, we repeated the first of the scans in the same sample spot for comparison. This gave qualitatively the same 2D results within the experimental noise limits as those shown, and the absolute decrease in 2D signal due to sample degradation was below 30%.

Theory and numerical simulations

The Frenkel exciton hamiltonian matrix elements, denoted by H_{jk} , were obtained by simultaneously fitting to the absorption and time-resolved 2D photon-echo spectra. The diagonal elements, H_{jj} , for BChl molecules $j = 1, \dots, 7$ (Fig. 2a), are 280, 420, 0, 175, 320, 360 and 260 cm^{-1} . The off-diagonal matrix elements are identical to those presented previously¹⁴, except that $H_{56} = H_{65}$ was reduced to 40 cm^{-1} because the corresponding diagonal frequencies were readjusted in the present work. The general nonlinear response functions were obtained^{3,22}, but the Laplace (stationary-phase approximation) method was used to calculate the corresponding 2D Fourier spectrum approximately. The site energy fluctuation was assumed to be uncorrelated with those of other sites. The frequency-frequency correlation function determining line broadening processes was expressed in terms of an ohmic-type spectral density, that is, $\rho(\omega) = (\lambda/\hbar\omega_c)\omega^{-1}\exp(-\omega/\omega_c)$, where

the cutoff frequency ω_c and the solvent reorganization energy λ were assumed to be 40 and 35 cm^{-1} , respectively. To calculate the rate constants we used modified Förster/Redfield theory^{26,27}. The rate constants are fully determined by the spectral density defined above and the electronic coupling constants. Here, the cutoff frequency dividing Förster and Redfield regimes was assumed to be 30 cm^{-1} so that if a given pair of pigments were coupled to each other weakly (less than 30 cm^{-1}) the excitation transfer process was treated as a Förster process. Denoting the exciton transport rate constant from the j th one-exciton state to the i th one-exciton state by k_{ij} , we found that $k_{21} = 0.12$, $k_{21} = 2.97$, $k_{13} = 0.12$, $k_{23} = 0.28$, $k_{24} = 5.38$, $k_{25} = 1.6$, $k_{26} = 0.22$, $k_{35} = 0.17$, $k_{37} = 1.6$, $k_{42} = 0.48$, $k_{45} = 2.0$, $k_{46} = 2.46$, $k_{54} = 0.91$, $k_{56} = 5.73$, $k_{57} = 0.16$, $k_{64} = 0.18$, $k_{65} = 0.92$, $k_{67} = 0.68$ and $k_{76} = 0.22$ (all in ps^{-1}). All other rate constants are smaller than 0.1 ps^{-1} . The initial populations of the seven exciton states were determined by using the experimental laser spectrum (Fig. 1d, red).

Received 29 November 2004; accepted 4 February 2005; doi:10.1038/nature03429.

1. Zewail, A. H. *Femtochemistry* (World Scientific, Singapore, 1994).
2. Asplund, M. C., Zanni, M. T. & Hochstrasser, R. M. Two-dimensional infrared spectroscopy of peptides by phase-controlled femtosecond vibrational photon echoes. *Proc. Natl Acad. Sci. USA* **97**, 8219–8224 (2000).
3. Mukamel, S. Multidimensional femtosecond correlation spectroscopies of electronic and vibrational excitations. *Annu. Rev. Phys. Chem.* **51**, 691–729 (2000).
4. Wright, J. C. Coherent multidimensional vibrational spectroscopy. *Int. Rev. Phys. Chem.* **21**, 185–255 (2002).
5. Khalil, M., Demirdöven, N. & Tokmakoff, A. Coherent 2D IR spectroscopy: Molecular structure and dynamics in solution. *J. Phys. Chem. A* **107**, 5258–5279 (2003).
6. Asbury, J. B. *et al.* Hydrogen bond dynamics probed with ultrafast infrared heterodyne-detected multidimensional vibrational stimulated echoes. *Phys. Rev. Lett.* **91**, 237402 (2003).
7. Cervetto, V., Helbing, J., Bredenbeck, J. & Hamm, P. Double-resonance versus pulsed Fourier transform two-dimensional infrared spectroscopy: An experimental and theoretical comparison. *J. Chem. Phys.* **121**, 5935–5942 (2004).
8. Jonas, D. M. Two-dimensional femtosecond spectroscopy. *Annu. Rev. Phys. Chem.* **54**, 425–463 (2003).
9. Fenna, R. E. & Matthews, B. W. Chlorophyll arrangement in a bacteriochlorophyll protein from *Chlorobium limicola*. *Nature* **258**, 573–577 (1975).
10. Li, Y.-F., Zhou, W., Blankenship, R. E. & Allen, J. P. Crystal structure of the bacteriochlorophyll *a* protein from *Chlorobium tepidum*. *J. Mol. Biol.* **271**, 456–471 (1997).
11. Blankenship, R. E. *Molecular Mechanisms of Photosynthesis* (Blackwell, Oxford, 2002).
12. Blankenship, R. E. & Matsuura, K. in *Light-Harvesting Antennas in Photosynthesis* (eds Green, B. R. & Parson, W. W.) 195–217 (Kluwer Academic, Dordrecht, 2003).
13. Savikhin, S., Buck, D. R. & Struve, W. S. Toward level-to-level energy transfers in photosynthesis: The Fenna–Matthews–Olson protein. *J. Phys. Chem. B* **102**, 5556–5565 (1998).
14. Vulto, S. I. E. *et al.* Exciton simulations of optical spectra of the FMO complex from the green sulfur bacterium *Chlorobium tepidum* at 6 K. *J. Phys. Chem. B* **102**, 9577–9582 (1998).
15. Vulto, S. I. E. *et al.* Excited state dynamics in FMO antenna complexes from photosynthetic green sulfur bacteria: A kinetic model. *J. Phys. Chem. B* **103**, 8153–8161 (1999).
16. Wendling, M. *et al.* The quantitative relationship between structure and polarized spectroscopy in the FMO complex of *Prosthecochloris aestuarii*: Refining experiments and simulations. *Photosynth. Res.* **71**, 99–123 (2002).
17. Lepetit, L. & Joffe, M. Two-dimensional nonlinear optics using Fourier-transform spectral interferometry. *Opt. Lett.* **21**, 564–566 (1996).
18. Tian, P., Keusters, D., Suzuki, Y. & Warren, W. S. Femtosecond phase-coherent two-dimensional spectroscopy. *Science* **300**, 1553–1555 (2003).
19. Cowan, M. L., Ogilvie, J. P. & Miller, R. J. D. Two-dimensional spectroscopy using diffractive optics based phased-locked photon echoes. *Chem. Phys. Lett.* **386**, 184–189 (2004).
20. Brixner, T., Stopkin, I. V. & Fleming, G. R. Tunable two-dimensional femtosecond spectroscopy. *Opt. Lett.* **29**, 884–886 (2004).
21. Brixner, T., Mancal, T., Stopkin, I. V. & Fleming, G. R. Phase-stabilized two-dimensional electronic spectroscopy. *J. Chem. Phys.* **121**, 4221–4236 (2004).
22. Cho, M. Nonlinear response functions for three-dimensional spectroscopies. *J. Chem. Phys.* **115**, 4424–4437 (2001).
23. Prall, B. S., Parkinson, D. Y., Fleming, G. R., Yang, M. & Ishikawa, N. Two-dimensional optical spectroscopy: Two-color photon echoes of electronically coupled phthalocyanine dimers. *J. Chem. Phys.* **120**, 2537–2540 (2004).
24. Tokmakoff, A. Two-dimensional line shapes derived from coherent third-order nonlinear spectroscopy. *J. Phys. Chem. A* **104**, 4247–4255 (2000).
25. Kwac, K. & Cho, M. Two-color pump-probe spectroscopies of two- and three-level systems: Two-dimensional line shapes and solvation dynamics. *J. Phys. Chem. A* **107**, 5903–5912 (2003).
26. Zhang, W. M., Meier, T., Chernyak, V. & Mukamel, S. Exciton-migration and three-pulse femtosecond optical spectroscopies of photosynthetic antenna complexes. *J. Chem. Phys.* **108**, 7763–7774 (1998).
27. Yang, M., Damjanovic, A., Vaswani, H. M. & Fleming, G. R. Energy transfer in photosystem I of cyanobacteria *Synechococcus elongatus*: Model study with structure-based semi-empirical Hamiltonian and experimental spectral density. *Biophys. J.* **85**, 140–158 (2003).
28. van Amerongen, H., Valkunas, L. & van Grondelle, R. *Photosynthetic Excitons* (World Scientific, Singapore, 2000).
29. Maznev, A. A., Nelson, K. A. & Rogers, T. A. Optical heterodyne detection of laser-induced gratings. *Opt. Lett.* **23**, 1319–1321 (1998).
30. Goodno, G. D., Dadusc, G. & Miller, R. J. D. Ultrafast heterodyne-detected transient-grating spectroscopy using diffractive optics. *J. Opt. Soc. Am. B* **15**, 1791–1794 (1998).

Acknowledgements We thank Y.-Z. Ma, L. Valkunas and M. Yang for discussions, and C. Goodhope for protein purification. The apparatus for 2D spectroscopy was constructed by I. V. Stiopkin and T.B. This work was supported by the DOE (at LBNL, UC Berkeley and Arizona State University), and by a CRIP grant to M.C. by KOSEF (Korea). T.B. thanks the German Science Foundation (DFG) for an Emmy Noether fellowship, and J.S. thanks the German Academic Exchange Service (DAAD) for a postdoctoral fellowship.

Competing interests statement The authors declare that they have no competing financial interests.

Correspondence and requests for materials should be addressed to G.R.F. (grfleming@lbl.gov) and M.C. (mcho@korea.ac.kr).

Decline of the marine ecosystem caused by a reduction in the Atlantic overturning circulation

Andreas Schmittner

College of Oceanic and Atmospheric Sciences, Oregon State University, 104 COAS Admin. Bldg, Corvallis, Oregon 97331, USA

Reorganizations of the Atlantic meridional overturning circulation were associated with large and abrupt climatic changes in the North Atlantic region during the last glacial period^{1–4}. Projections with climate models suggest that similar reorganizations may also occur in response to anthropogenic global warming^{5–7}. Here I use ensemble simulations with a coupled climate–ecosystem model of intermediate complexity to investigate the possible consequences of such disturbances to the marine ecosystem. In the simulations, a disruption of the Atlantic meridional overturning circulation leads to a collapse of the North Atlantic plankton stocks to less than half of their initial biomass, owing to rapid shoaling of winter mixed layers and their associated separation from the deep ocean nutrient reservoir. Globally integrated export production declines by more than 20 per cent owing to reduced upwelling of nutrient-rich deep water and gradual depletion of upper ocean nutrient concentrations. These model results are consistent with the available high-resolution palaeorecord, and suggest that global ocean productivity is sensitive to changes in the Atlantic meridional overturning circulation.

The climatic consequences of Atlantic meridional overturning (AMO) reorganizations have been intensely documented in recent decades^{1–4}. Temperature oscillations in Greenland, recorded in the isotopic composition of the ice, show rapid warmings of about 10°C , known as Dansgaard–Oeschger events, coincident with abrupt increases of sea surface temperature (SST) and sea surface salinity (SSS) in the North Atlantic. During the cold (stadial) phases of the oscillations, deep water formation in the North Atlantic was partially or entirely stopped³, leading to reduced northward heat transport by the ocean. Observed spatial patterns, amplitudes and phasing of temperature changes associated with Dansgaard–Oeschger oscillations can be successfully reproduced with coupled climate models forced with disturbances of the Atlantic freshwater budget⁴. However, the consequences of AMO changes for the marine ecosystem have not yet been quantified on a global scale. This will be particularly important, as projections of future climate change indicate that the AMO could weaken or even disappear in the coming centuries owing to anthropogenic greenhouse gas emissions^{5–7}. Here I examine the impact of changes in ocean circulation on the marine ecosystem.

A climate model of intermediate complexity is used, including